

1                    **Empirical Green’s Function Retrieval using**  
2                    **Cross-correlation of Ambient Noise Correlations ( $C^2$ )**

3                    **Yunfeng Chen<sup>1</sup>, and Erdinc Saygin<sup>1,2</sup>**

4                    <sup>1</sup>Deep Earth Imaging, Future Science Platform, CSIRO, Perth, WA, 6151, Australia

5                    <sup>2</sup>Department of Physics, School of Physics, Mathematics and Computing, University of Western  
6                    Australia, Perth, Western Australia, Australia

7                    **Key Points:**

- 8                    • An effective higher-order correlation technique is developed to extract the empir-  
9                    ical Green’s functions (EGFs) from asynchronous networks.
- 10                    • Our technique cross-correlates the deterministic wavefield from virtual sources and  
11                    provides high-quality EGF estimates.
- 12                    • Seismic tomography using asynchronous EGFs offers new constraints to areas under-  
13                    sampled by conventional ambient noise imaging methods.

14                    This is a non-peer reviewed preprint submitted to EarthArXiv.

## Abstract

Empirical Green's function (EGF) retrieval commonly relies on cross-correlating the long-term ambient seismic wavefield that is simultaneously recorded at multiple stations. Recent studies have demonstrated observationally that cross-correlating the coda of ambient noise cross-correlation functions ( $C^3$ ) enables reconstruction of the EGFs, regardless of the operating time of the stations. In this study, we develop a new technique to perform correlation of cross-correlation functions ( $C^2$ ), thus permitting the reconstruction of asynchronous EGFs. Our approach exploits the deterministic wavefield rather than the diffusive codas that may be affected by incoherent energy under non-ideal (e.g., sparse, noisy and short-duration) network configurations. We demonstrate the robustness of  $C^2$  by retrieving asynchronous EGFs between 1) nearby stations and 2) distant temporary arrays from southern Australia. The accuracy of the EGFs from  $C^2$  are examined by analyzing seismic tomography of Rayleigh wave group velocities and benchmarking them with the results from conventional ambient noise imaging. The additional ray paths from asynchronous  $C^2$  functions provide better illumination of small-scale crustal structures beneath the regional network. In the larger scale example, involving two asynchronous arrays, the implementation of the  $C^2$  method offers new constraints to the sparsely sampled region of the southern Australian offshore. The resulting velocity model agrees well with the independent structural constraints from individual seismic array studies and sedimentary thickness measurements. This study demonstrates that  $C^2$  is a promising tool for integrating transportable arrays deployed at different times and can greatly benefit the effort of improving seismic data coverage and resolution in crustal imaging.

## Plain Language Summary

Seismic waves propagating between a pair of stations can be obtained by cross-correlating the long-term random (noisy-looking) signals simultaneously recorded at two stations. Earlier studies have shown that surface waves propagating between two stations, operated at different times (i.e., asynchronous), can also be obtained by cross-correlating the weak-amplitude coda waves trailing the strong surface waves in the correlation function. In this study, we develop a new method that directly utilizes the energetic surface waves, rather than just the codas, to extract the seismic waves between asynchronous stations. This method is more robust than the earlier proposed coda-wave based approach, espe-

46 cially when dealing with sparse, noisy and short-duration seismic networks. We apply  
47 this new method at different length scales from nearby stations to two far apart, sep-  
48 arated networks to demonstrate its superior performance to the traditional approach.  
49 The new method can greatly improve data sampling and the resolution of seismic im-  
50 age of subsurface structures.

## 51 **1 Introduction**

52 Seismic interferometry, commonly known as ambient noise cross-correlation in pas-  
53 sive seismology, has been widely applied to probe the structure of the Earth’s interior  
54 at various scales over the past two decades (e.g., Shapiro & Campillo, 2004; Yao et al.,  
55 2006; Lin et al., 2007, 2008; Yang et al., 2007; Stehly et al., 2009; Saygin & Kennett, 2012;  
56 Kao et al., 2013; Ward et al., 2013; Rawlinson et al., 2014; Porritt et al., 2016). Both  
57 experimental and theoretical studies (e.g., Lobkis & Weaver, 2001; Weaver & Lobkis, 2001;  
58 Shapiro & Campillo, 2004) have demonstrated that sufficient time-averaging of the cross-  
59 correlation of diffuse wavefields recorded at two receivers effectively converge into the  
60 interstation empirical Green’s function (hereafter EGF) (see Snieder & Larose, 2013; Campillo  
61 et al., 2014; Boschi & Weemstra, 2015, for reviews). Conventionally, ambient noise cross-  
62 correlation relies on the acquisition of equipartioned seismic wave energy from simulta-  
63 neously acting sources (Wapenaar et al., 2010), which imposes a temporal constraint that  
64 two stations need to operate simultaneously over a period of time. In recent years, meth-  
65 ods have been proposed to reconstruct EGFs by cross-correlating the coda of the cor-  
66 relation functions (hereafter  $C^3$ ) extracted from the ambient noise (e.g., Stehly et al.,  
67 2008; Froment et al., 2011; Ma & Beroza, 2012; Sheng et al., 2018). Such an approach  
68 has been largely inspired by the earthquake coda interferometry that utilizes scattered  
69 wave energy containing coherent information about the elastic response of the Earth (Campillo  
70 & Paul, 2003). An underlying assumption of the  $C^3$  approach is that the long-term stack-  
71 ing of correlation functions produces stable, predominantly time-invariant coda waves  
72 (Ma & Beroza, 2012), which permits extracting the EGFs between asynchronous stations  
73 from the coherent coda energy acquired at different times. The additional ray paths from  
74 the asynchronous EGFs enable improvement of the resolution of crustal imaging (Spica  
75 et al., 2016; Ansaripour et al., 2019).

76 Aside from using diffuse wavefields, another branch of seismic interferometry takes  
77 advantage of the deterministic signals from controlled (e.g., Schuster et al., 2004; Bakulin

78 & Calvert, 2006; Schuster, 2009) or earthquake sources (e.g., Curtis et al., 2009, 2012).  
79 This method generally integrates the correlation functions over the (known) distributed  
80 sources (Wapenaar et al., 2010). An intriguing implementation is source-receiver inter-  
81 ferometry (Curtis & Halliday, 2010) that retrieves the EGF between a source-receiver  
82 pair using the deterministic energy propagating from/to a set of surrounding receivers.  
83 Its application is not restricted to synchronous source-receiver pairs, thus, the virtual  
84 seismogram of an earthquake can be constructed on receivers deployed before or after  
85 the event, as long as the recordings are made using a few qualified backbone stations (Curtis  
86 et al., 2012).

87 Both the ambient noise coda-wave correlation (i.e.,  $C^3$ ) and source-receiver inter-  
88 ferometry techniques provide a form of temporal redatuming, whereby it is possible to  
89 reconstruct the EGFs between asynchronous station-station (earthquake) pairs. In this  
90 study, we extend beyond these two methods and examine the feasibility of reconstruct-  
91 ing EGFs from the deterministic wavefield extracted from ambient noise data. Specif-  
92 ically, we show that reliable EGF estimates are achievable from higher-order correlations  
93 that perform the cross-correlation of correlation functions (hereafter  $C^2$ ) from surround-  
94 ing virtual sources (i.e., backbone stations). We demonstrate the effectiveness of the  $C^2$   
95 technique using the data collected from two temporary networks deployed in southern  
96 Australia, operated five years apart and separated by a distance of approximately 1500  
97 km (Figure 1). We show that the  $C^2$  method can robustly reconstruct the EGFs between  
98 nearby asynchronous stations and can easily be scaled up to achieve continental-scale  
99 applications involving distant temporary arrays. Benefiting from the asynchronous EGFs,  
100 the surface wave travel-time tomography offers new constraints to the southern Australian  
101 offshore, a region poorly resolved by conventional ambient-noise based methods.



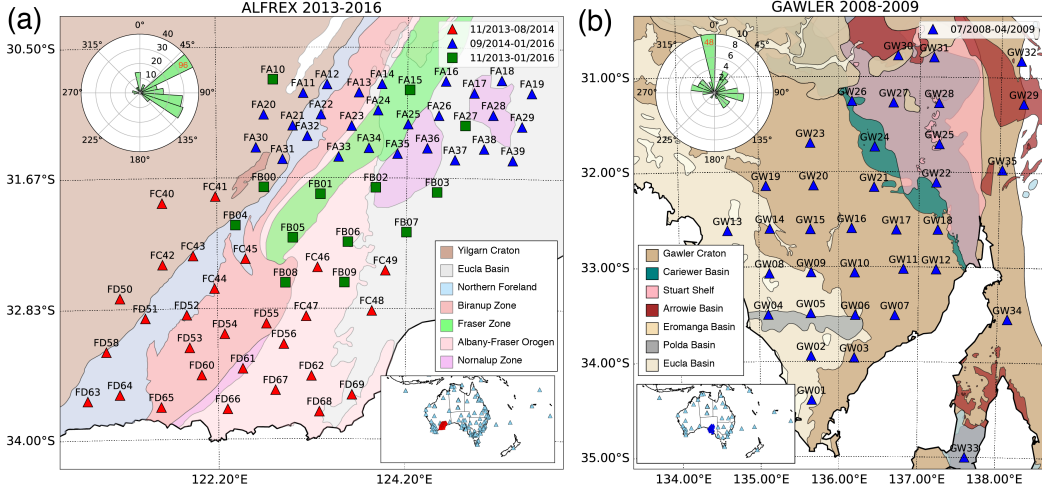


**Figure 1.** Spatiotemporal distribution of (a) ALFREX and (b) GAWLER seismic networks superimposed on regional geological maps of southern Australia. The crustal domains are colored to show the complex regional tectonic structures. The rose diagram shows the azimuthal distribution of virtual source stations used in the empirical Green’s function ( $C^2$ ) retrieval in the respective test cases. The radial axis is clipped for a better illustration and the number of stations in the dominating direction are labeled on the bar. In the inset map, the locations of permanent seismic stations acting as virtual sources are marked with the cyan triangles and the ALFREX and GALWER networks are highlighted in red and blue.

## 2 Empirical Green’s function retrieval

The computation of  $C^2$  is a two-stage process. The first step of our high-order cross-correlation scheme is to perform the conventional ambient noise cross-correlation (Figure 2a) that is mathematically expressed as

$$G(x, s, t) \simeq u(x, t) \otimes u(s, t), \quad (1)$$

where  $G(x, s, t)$  is the EGF between stations  $x$  and  $s$  at time  $t$ ,  $u(x, t)$  and  $u(s, t)$  are the corresponding wavefields recorded at two stations and  $\otimes$  represents the cross-correlation operator. This process turns station  $s$  into a virtual source (Figure 2b). Although equation (1) does not explicitly differentiate the source types (i.e., diffuse vs. deterministic) in the seismic recordings, ambient noise imaging usually utilizes the stochastic signals (e.g., noise) and removes the contaminating deterministic part (e.g., earthquakes) before cross-correlation (Bensen et al., 2007). Later, we show that this operation is not necessary for extracting EGFs using higher-order cross-correlations. To compute cross-correlation

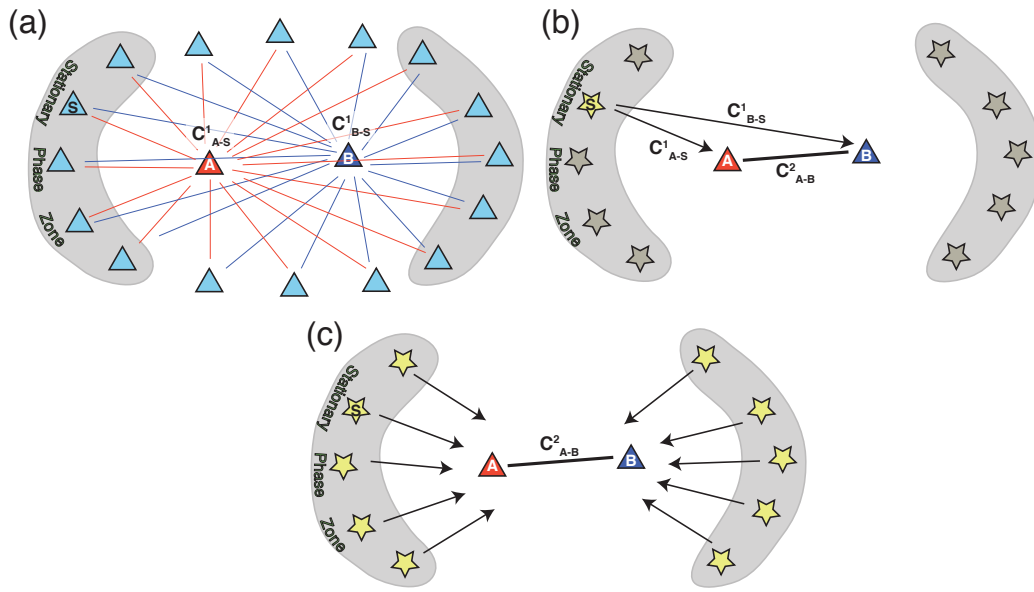


**Figure 2.** Cartoon illustrates the concept of  $C^2$ . (a) Ambient noise correlations are performed between two temporary stations ( $A$  and  $B$ ) and the surrounding permanent stations ( $S$ ). This process turns the permanent stations into virtual sources. (b) The deterministic surface waves emitted from a virtual source station  $S$  (star) are recorded at stations  $A$  and  $B$ , which are then cross-correlated to obtain a  $C^2$  function. (c) The cross-correlations are conducted for all virtual sources located within the stationary phase zone (shaded grey) that contribute constructively to the stacking.

114 functions (hereafter  $C^1$ ) we cut the continuous seismic recordings into one hour segments  
 115 with a 50% overlap between consecutive windows. After removing the mean and linear  
 116 trend, we down-sample the data to 5 Hz and apply a bandpass filtering with corner fre-  
 117 quencies at 150 sec and 0.5 sec. The processed (synchronous) time series from two sta-  
 118 tions are cross-correlated and stacked to obtain the final  $C^1$  estimate.

119 In the second step, we perform EGF retrieval by cross-correlating the correlation  
 120 functions. This is formulated in the time domain as

$$G(x_B, x_A, t) \simeq \frac{1}{N} \sum_{i=1}^N G(x_B, s_i, t) \otimes G(x_A, s_i, t), \quad (2)$$

121 where  $G(x_B, s_i, t)$  and  $G(x_A, s_i, t)$  are the EGFs approximated using equation (1) be-  
 122 tween temporary stations  $x_A$  or  $x_B$  and a virtual source station  $s_i$ , and the summation  
 123 of correlation functions over  $N$  virtual sources produces  $G(x_B, x_A, t)$ , the EGF between  
 124  $x_A$  and  $x_B$  (Figure 2c). The two temporary stations (i.e.,  $x_A$  and  $x_B$ ) need not to be  
 125 operating at the same time as long as the EGFs from a common virtual source (i.e.,  $s_i$ )  
 126 exist, which is typically one of the permanent stations from the backbone seismic net-  
 127 work (Figure 1). Therefore, equation (2) provides a framework for reconstructing EGFs  
 128 between asynchronous stations. In data processing, we select  $C^1$  functions with at least  
 129 three months of stacking to ensure the signal quality; no prior temporal or frequency nor-  
 130 malizations are required. The  $C^1$  functions are divided into causal and acausal signals,  
 131 and cross-correlation is applied on each segment separately. The resulting two correla-  
 132 tion functions (i.e., causal-causal and time reversed acausal-acausal correlations) are stacked  
 133 to form a  $C^2$  estimate. The final EGF between the two stations is obtained by stack-  
 134 ing the normalized  $C^2$  functions from all virtual sources.

### 135 3 Data

136 We apply the proposed higher-order cross-correlation method ( $C^2$ ) to retrieve EGFs  
 137 at two length scales 1) asynchronous station pairs within a regional array and 2) two dis-  
 138 tant temporary networks with different operating periods (see Figure 1). The first ex-  
 139 ample uses the recordings from the ALFREX network that consists of two subarrays, each  
 140 sampling a part of the Albany-Fraser orogen in southwestern Australia at different time  
 141 periods, as well as 13 semi-permanent stations operating throughout the acquisition pe-  
 142 riod (Figure 1a). This network configuration is representative of a regional seismic sur-  
 143 vey with a campaign-mode deployment (e.g., Transportable component of USArray). In

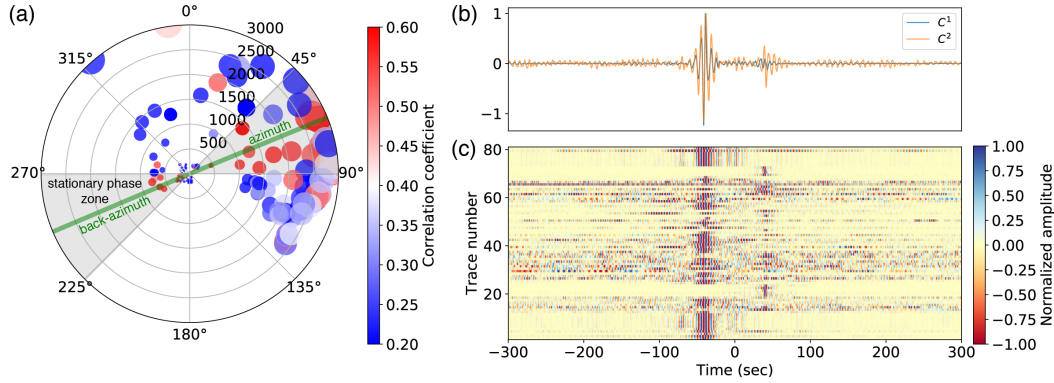


**Figure 3.** Comparison of the empirical Green’s functions retrieved from  $C^1$  and  $C^2$  approaches for the station pair FB07-FB08 within ALFREX. (a) Azimuthal and distance distribution of the correlation coefficient between  $C^1$  and  $C^2$  from individual virtual source. The green line indicates the directions of azimuth and back-azimuth of the selected station pair. The gray shades highlight the stationary phase zone that contributes constructively to the stacking. (b) Waveform comparison between  $C^1$  (orange) and stacked  $C^2$  (blue) using virtual sources within the stationary phase zone. The waveforms are filtered between 2 and 20 sec. (c) Normalized  $C^2$  function from each virtual source contributes to the stack in (b).

144 the larger scale implementation, we select a distant seismic network (GAWLER) deployed  
 145 approximately 1500 km to the east of ALFREX near the Gawler craton in southern Aus-  
 146 tralia (Figure 1b). Stations of the GALWER network were operated synchronously be-  
 147 tween 2008-2009 but did not overlap in time with the ALFREX deployment (2013-2016).  
 148 The large separation distance and asynchronous operations of the two arrays present great  
 149 challenges when reconstructing the inter-array EGFs with conventional ambient noise  
 150 or coda-wave based correlation methods. To implement  $C^2$ , we incorporate all the avail-  
 151 able permanent stations near the Australian continent as virtual sources (see Figure 1).

## 152 4 Results

### 153 4.1 Empirical Green’s function retrieval between asynchronous stations

154 We compute  $C^2$  between all possible station pairs within the ALFREX network  
 155 that include both synchronous and asynchronous setups. The synchronous EGFs are ex-  
 156 tracted between subarrays and 13 semi-permanent stations for a direct comparison with  
 157 the EGFs obtained from the ambient noise fields (i.e.,  $C^1$ ) (Figure 1a). We show a sam-

158 ple  $C^2$  measurement between a pair of stations located in the center of the ALFREX ar-  
 159 ray to ensure a balanced azimuthal coverage of the virtual sources (Figure 3). We com-  
 160 pute the correlation coefficient of  $C^2$  from each virtual source with  $C^1$  as a function of  
 161 distance and azimuth (Figure 3a). The distribution of the correlation coefficient shows  
 162 a strong dependence on azimuth: higher values are observed in the directions of azimuth  
 163 and back-azimuth of the selected station pair, while lower values are distributed perpen-  
 164 dicular, consistent with the stationary phase approximation (Snieder, 2004; Snieder et  
 165 al., 2008). By comparison, the dependency of the correlation coefficient on distance is  
 166 weak, which may be affected by factors such as site condition, local structures and am-  
 167 bient noise source distributions. We define the stationary phase zone as a 45-degree az-  
 168 imuthal bin centering on the direction of inter-station line and perform stacking of  $C^2$   
 169 functions using only virtual sources within this regime. The stacked  $C^2$  is highly con-  
 170 sistent with the corresponding  $C^1$  with a correlation coefficient of 0.86 (Figure 3b). Each  
 171 individual  $C^2$  from a contributing source shows a clear Rayleigh-type surface wave en-  
 172 ergy on either a positive or negative time axis, depending on the direction of the source  
 173 (Figure 3c).

174 We use stations from several long-operating networks distributed across the Aus-  
 175 tralian continent, which provides approximately 180 virtual sources in  $C^2$  calculation (Fig-  
 176 ure 4a). The spatial distribution of virtual sources, particularly their azimuthal cover-  
 177 age relative to the temporary stations, strongly affects the quality and reliability of the  
 178 retrieved EGFs from  $C^2$  (see Figure 3). Thus, we only select the virtual sources that sat-  
 179 isfy the stationary phase constraint; on average 50 stations contribute to the stacking  
 180 of  $C^2$ . The resulting EGFs ( $C^2$ ) show consistent surface wave arrivals characterized by  
 181 1) a similar move-out velocity to that of the EGF estimates of  $C^1$  (Figure 4b) and 2)  
 182 a comparable waveform quality between synchronous and asynchronous station pairs at  
 183 the overlapped distances (Figure 4c).

## 184 **4.2 Dispersion measurements and ambient noise tomography**

185 We examine the robustness of the EGFs from  $C^2$  by computing the surface wave  
 186 dispersion curve. The frequency-dependent Rayleigh wave travel times are determined  
 187 by FTAN (e.g., Levshin & Ritzwoller, 2001). This method applies a series of narrow-band  
 188 Gaussian filters with varying center frequencies to the analytical signal of the cross-correlation  
 189 function. The amplitude of the filtered signal defines an envelope function of the sur-

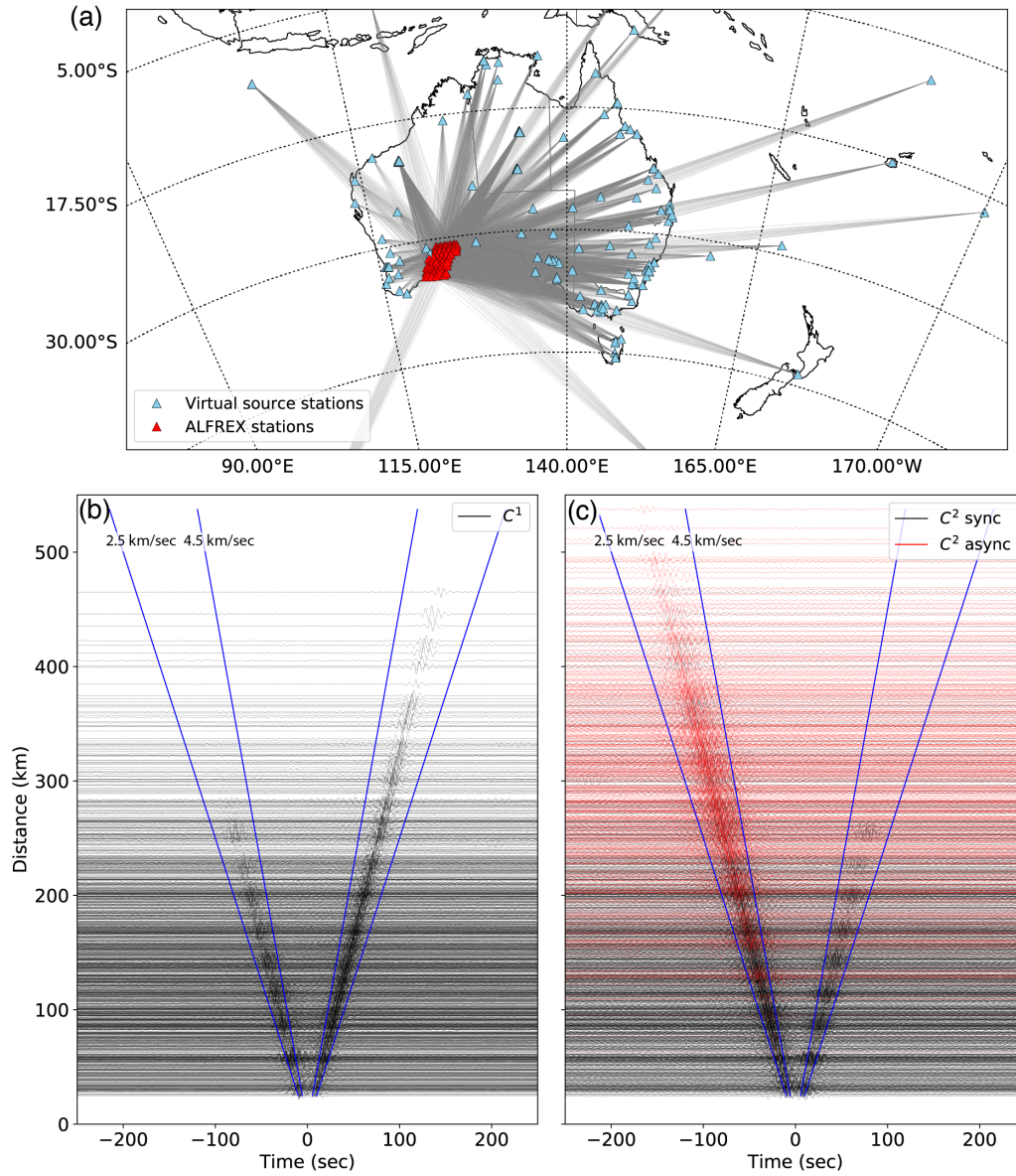


**Figure 4.** Empirical Green's functions (EGFs) of station pairs within the ALFREX network. (a) The ray-paths between virtual sources (cyan) and ALFREX stations (red) used in calculation of  $C^2$ . (b) The EGFs extracted using the  $C^1$  approach. The waveforms are normalized to unity and filtered between 5 and 20 sec. The blue lines mark the respective move-out velocities of 2.5 and 4.5 km/sec, corresponding to the expected range of speed for surface waves in southwestern Australia (Saygin & Kennett, 2012). (c) The EGFs between synchronous (black) and asynchronous (red) station pairs from  $C^2$ .



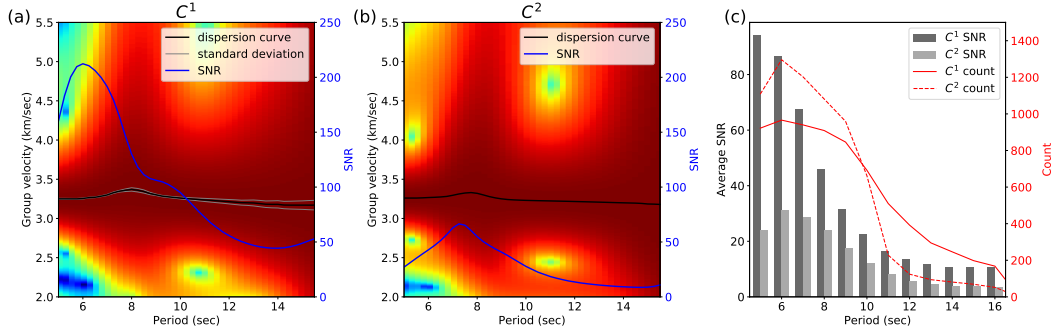


**Figure 5.** Group velocity measurements of (a)  $C^1$  and (b) synchronous  $C^2$  functions between the station pair FA10-FA15. The black line shows the dispersion curve and the blue line shows the signal-to-noise ratio (SNR) of the cross-correlation function. The uncertainty of the dispersion curve of  $C^1$  is determined by the standard deviation of the measurements on the three-month stacking of  $C^1$  functions (e.g., January-March, February-April etc.). (c) The histogram of average SNR of  $C^1$  (dark grey) and  $C^2$  (light grey) functions at each period. The red solid line shows the number of dispersion measurements of  $C^1$  with  $\text{SNR} > 10$  and the corresponding result for  $C^2$  is indicated by the dashed line.

190 face wave, from which the dispersion curve can be retrieved by tracking the peak loca-  
 191 tion of the envelope at each period. The dispersion curves of  $C^1$  and  $C^2$  functions be-  
 192 tween a sample station pair (FA10-FA15) are highly consistent within the frequency band  
 193 of interest (4-16 sec) (Figure 5). The average discrepancy is 0.01 km/sec, which is well  
 194 below the uncertainty range (0.02 km/sec) of the dispersion measurement of  $C^1$  that re-  
 195 sults from the temporal variation in the EGF (Figures 5a). We further assess the qual-  
 196 ity of dispersion measurements based on the signal-to-noise ratio (SNR). We define the  
 197 SNR as the ratio between the maximum absolute amplitude of the surface wave and the  
 198 standard deviation of the noise in a 500 sec window that starts 500 sec after the surface  
 199 wave arrival. For the selected station pair, the SNRs of the  $C^1$  and  $C^2$  functions both  
 200 peak at short periods ( 7 sec) and decrease rapidly towards longer periods (Figures 5a  
 201 and 5b). The SNR value of the  $C^1$  function is significantly higher than that of  $C^2$  at all  
 202 periods, which is expected when  $C^1$  emerges from a sufficiently-averaged ambient noise  
 203 field. The average SNR of dispersion measurements of all station pairs shows a similar  
 204 decaying pattern (Figure 5c). For both  $C^1$  and  $C^2$  functions, the majority of high-quality  
 205 measurements ( $\text{SNR} > 10$ ) are concentrated between 5-9 sec, which approximately coin-  
 206 cides with the frequency band of the primary microseism (Campillo et al., 2014), and

207 the number decreases with increasing period (Figure 5c). The inclusion of asynchronous  
 208 station pairs leads to a greater number of measurements of  $C^2$  at periods below 10 sec,  
 209 beyond which the number decreases quickly to about half of the  $C^1$  results (Figure 5c).  
 210 The sharp decrease of  $C^2$  measurements at 10 sec is limited mainly by the instrument  
 211 type of the ALFREX stations, the majority of which are equipped with short-period (1  
 212 Hz) sensors. The cross-correlation involving a short-period station produces incoherent  
 213 signals at longer periods. This effect is amplified in the  $C^2$  function because of the mul-  
 214 tiple (two-times) cross-correlations of narrow band signals.

### 215 **4.3 Ambient noise tomography with EGFs from $C^2$**

216 We perform ambient seismic tomography (ANT) to verify that the EGFs from  $C^2$   
 217 are indeed composed of physical signals carrying information on the Earth’s structure  
 218 and are not processing artifacts. We conduct four groups of inversions considering the  
 219 distinctive ray-path constraints of  $C^1$  and  $C^2$  functions (Figure 6). The  $C^1$  function mainly  
 220 offers short-distance EGFs between nearby stations (Figure 6a) with the majority of inter-  
 221 station distances being less than 250 km (see Figure 4b). The  $C^2$  approach enables re-  
 222 construction of the EGFs between both synchronous and asynchronous station pairs. The  
 223 former possesses a similar ray-path coverage to that of  $C^1$  with a slightly lower sampling  
 224 density (Figure 6b), whereas the asynchronous case provides primarily long-distance (200-  
 225 450 km) EGFs connecting the two subarrays (Figure 6c). Thus, the combined ray-paths  
 226 from  $C^1$  and asynchronous  $C^2$  provide complementary (short vs. long wavelength) con-  
 227 straints to the subsurface structures (Figure 6d).

228 We invert the 5-sec dispersion measurements for group velocities based on an it-  
 229 erative non-linear inversion scheme that applies the fast-matching method for wavefront  
 230 tracking (Rawlinson & Kennett, 2004). To ensure the accuracy of the dispersion mea-  
 231 surement, travel times that deviate largely from the linear trend (i.e., more than two stan-  
 232 dard deviation) of the time-distance relationship are considered to be outliers and dis-  
 233 carded from the subsequent inversion (supplementary Figure S3). The study area is pa-  
 234 rameterized into a regular grid of  $31 \times 31$  nodes, which approximates to a cell size of 20  
 235 km in both directions. A constant velocity of 3.24 km/sec is assigned to each node lo-  
 236 cation as the initial value. We follow the damping and smoothing criteria from Sippl et  
 237 al. (2017) for the inversions of  $C^1$ , synchronous  $C^2$  and the joint  $C^1$  and asynchronous  
 238  $C^2$  functions considering a similar ray-path coverage (Figure 6). Lower values are adopted



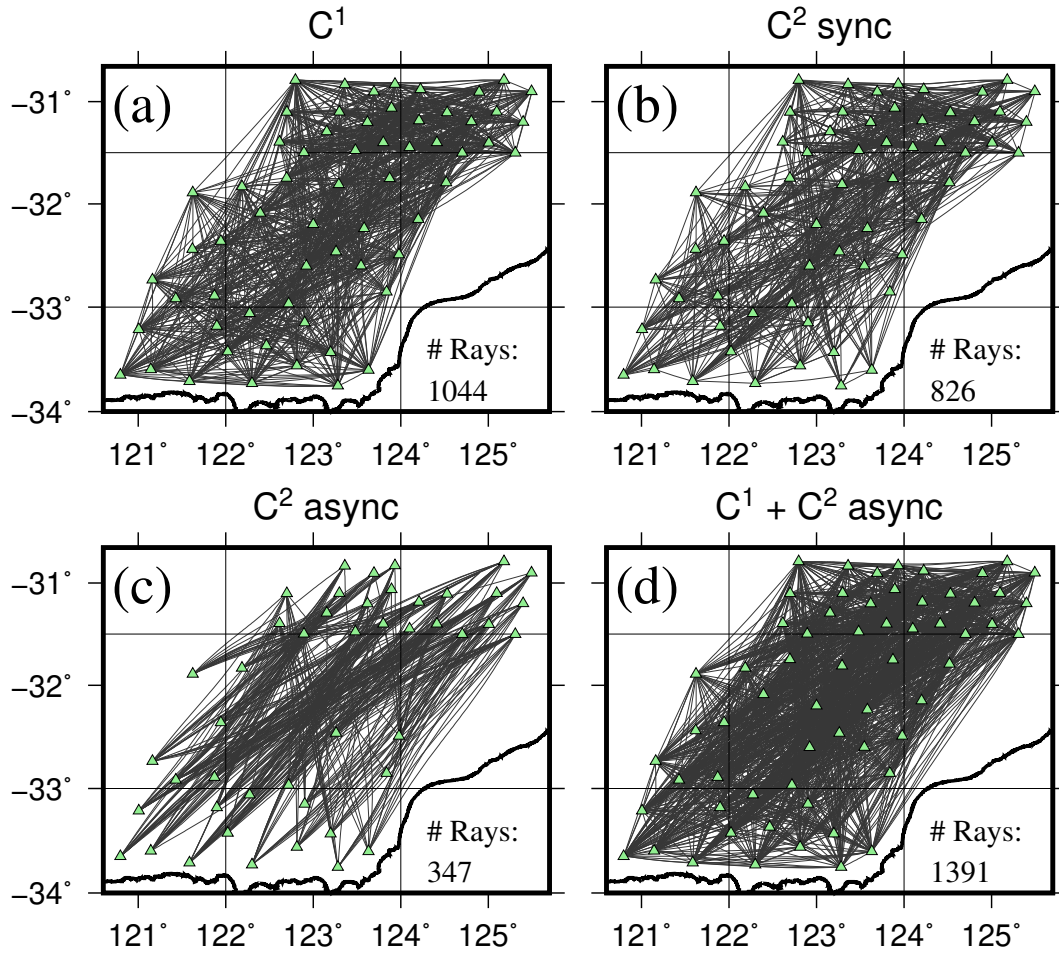


**Figure 6.** The ray-path coverages at 5 sec of (a)  $C^1$ , (b) synchronous  $C^2$ , (c) asynchronous  $C^2$  and (d)  $C^1$  and asynchronous  $C^2$  functions from ALFREX. Only ray paths with robust travel-time measurements (i.e., within one standard deviation of the linear regression of time-distance curve) are preserved.

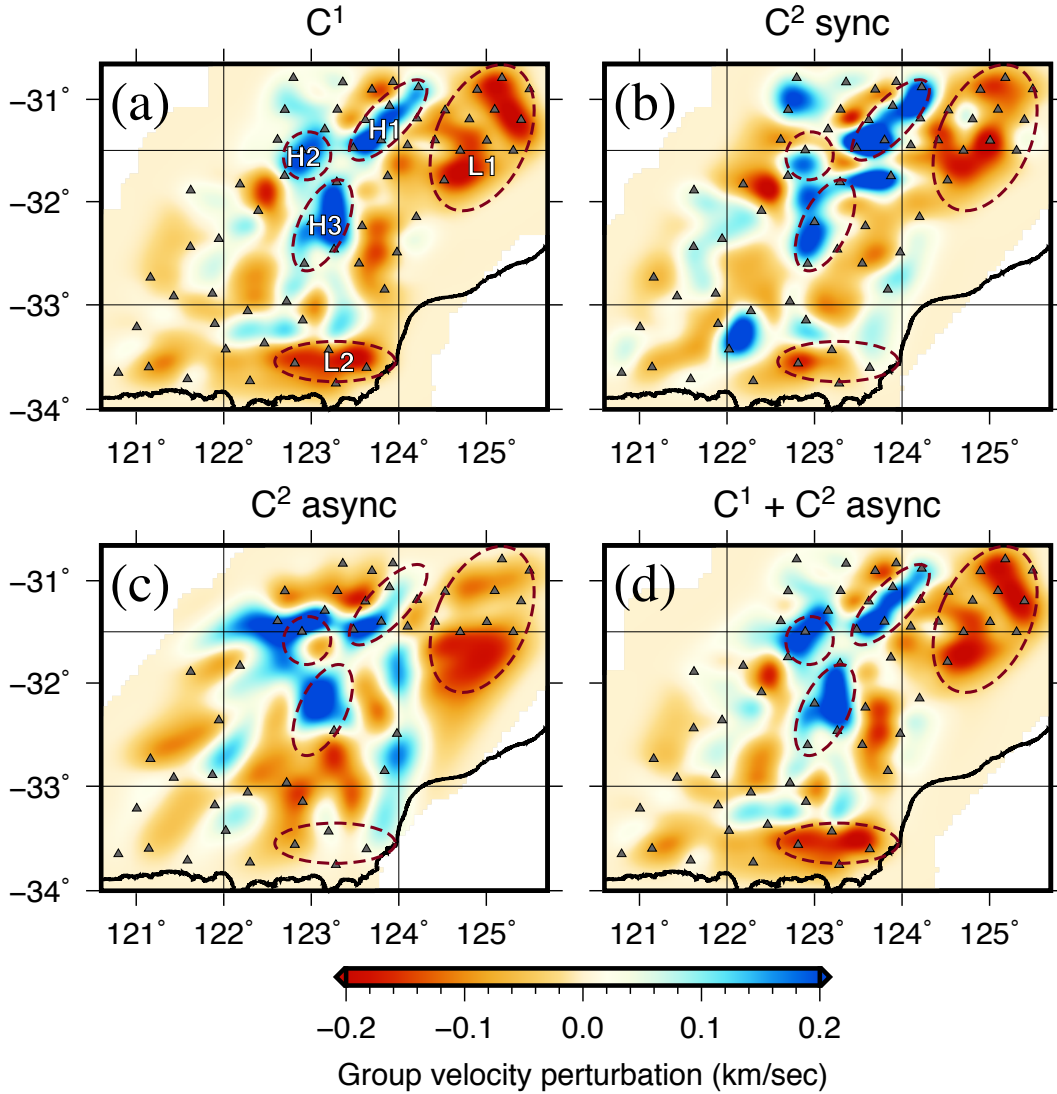


**Figure 7.** Group velocities at 5 sec beneath the ALFREX network inverted using (a)  $C^1$ , (b) synchronous  $C^2$ , (c) asynchronous  $C^2$  and (d)  $C^1$  and asynchronous  $C^2$  functions. The velocities are plotted in perturbation relative to the regional mean of 3.24 km/sec. The circled areas highlight the major high (H1-H3) and low (L1-L2) velocity structures discussed in the text.

239 for the inversion of asynchronous  $C^2$  functions to account for the intrinsic smoothing ef-  
 240 fect imposed by the long-distance ray-paths (Figure 6c). The resulting  $C^1$  tomogram shows  
 241 a dominating NE-SW striking high-velocity structure with three distinctive clusters (H1-  
 242 H3) that are bound by a broad low-velocity zone (L1) to the east and a smaller low-velocity  
 243 zone (L2) to the south (Figure 7a), consistent with the observations from the study by  
 244 Sippl et al. (2017). The inversion of synchronous  $C^2$  functions largely confirms the ve-  
 245 locity pattern observed in the  $C^1$  result. However, the shape of high-velocity structures  
 246 (H2 and H3) are less-well constrained and the smaller low-velocity zone (L2) is recov-  
 247 ered at a lower amplitude because of reduced ray-path density in these regions (Figure  
 248 7b). The asynchronous result successfully captures the large-scale structural variation  
 249 of the juxtaposed high and low velocities. The recovery of three high-velocity structures  
 250 is in reasonable agreement with the  $C^1$  result (Figure 7c). The larger low-velocity zone  
 251 (L1) is generally well resolved, except at the northern tip. In contrast, the smaller-scale  
 252 low velocity anomaly L2 is characterized by close to average wave speeds, which poten-  
 253 tially represents an inversion artifact arising from a lack of crisscrossing ray-paths in that  
 254 region (Figure 6c). The combined dataset that consists of the  $C^1$  and asynchronous  $C^2$   
 255 functions leads to 1) more crisscrossing ray-paths in the center of the network and 2) an  
 256 increased number of rays sampling the eastern and western flanks of the model (com-  
 257 pare Figures 6a and 6d). The overall improvement is subtle as there is a dominating con-  
 258 tribution from  $C^1$  functions, yet the resulting model exhibits a better recovery of small-  
 259 scale anomalies (e.g., H2) and more distinct velocity variation across the array (e.g., shaper  
 260 contrast between H3 and surrounding regions) (Figure 7d).

#### 261 **4.4 Empirical Green’s function retrieval between distant asynchronous** 262 **networks**

263 The example of ALFREX demonstrates the robustness of the  $C^2$  method in retriev-  
 264 ing EGFs within a regional-scale temporary network. A more challenging test is performed  
 265 on two distant arrays (ALFREX and GAWLER), where the inter-array  $C^1$  is not avail-  
 266 able because of the non-overlapping deployment periods of the two temporary networks.  
 267 The dominating east-west orientation of the ray-paths makes the permanent stations lo-  
 268 cated along the eastern and western coasts of Australia the most useful virtual sources  
 269 for constructing  $C^2$ , on average 22 sites contribute to the EGF retrieval (Figure 8a). De-  
 270 spite a significantly smaller number of virtual sources employed in the extractions com-

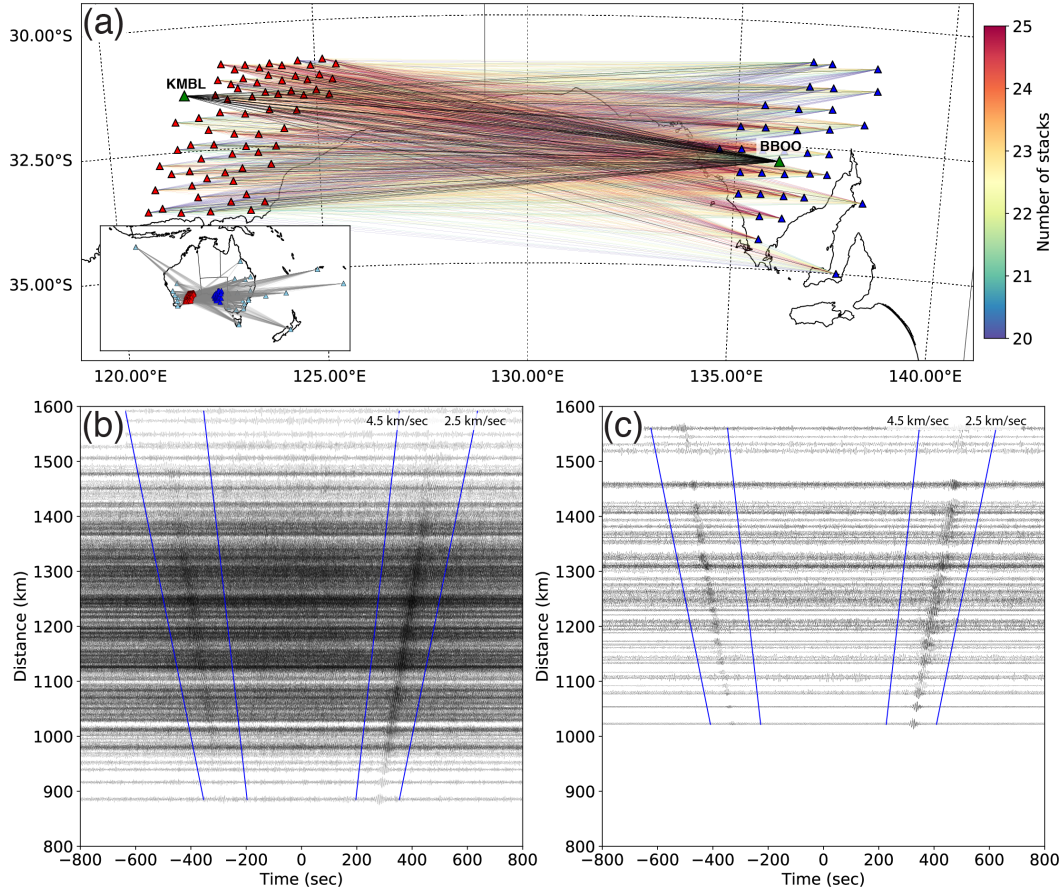


**Figure 8.** Empirical Green’s function (EGF) retrieval using two distant temporary networks of ALFREX and GAWLER. (a) The inter-array ray paths between stations from the two networks color-coded with the number of virtual sources used in the stack. The green triangles mark two nearby permanent stations (KMBL and BBOO) that are used to compute  $C^1$ . The ray paths connecting the permanent station to the temporary stations in the opposite network are shown by the black lines. The inset map shows the distribution of virtual source stations (cyan triangles). (b) The inter-array EGFs retrieved using  $C^2$ . (c) The EGFs retrieved using  $C^1$  between the selected permanent stations and temporary arrays shown in (a). All waveforms are normalized and filtered between 2 and 20 sec.

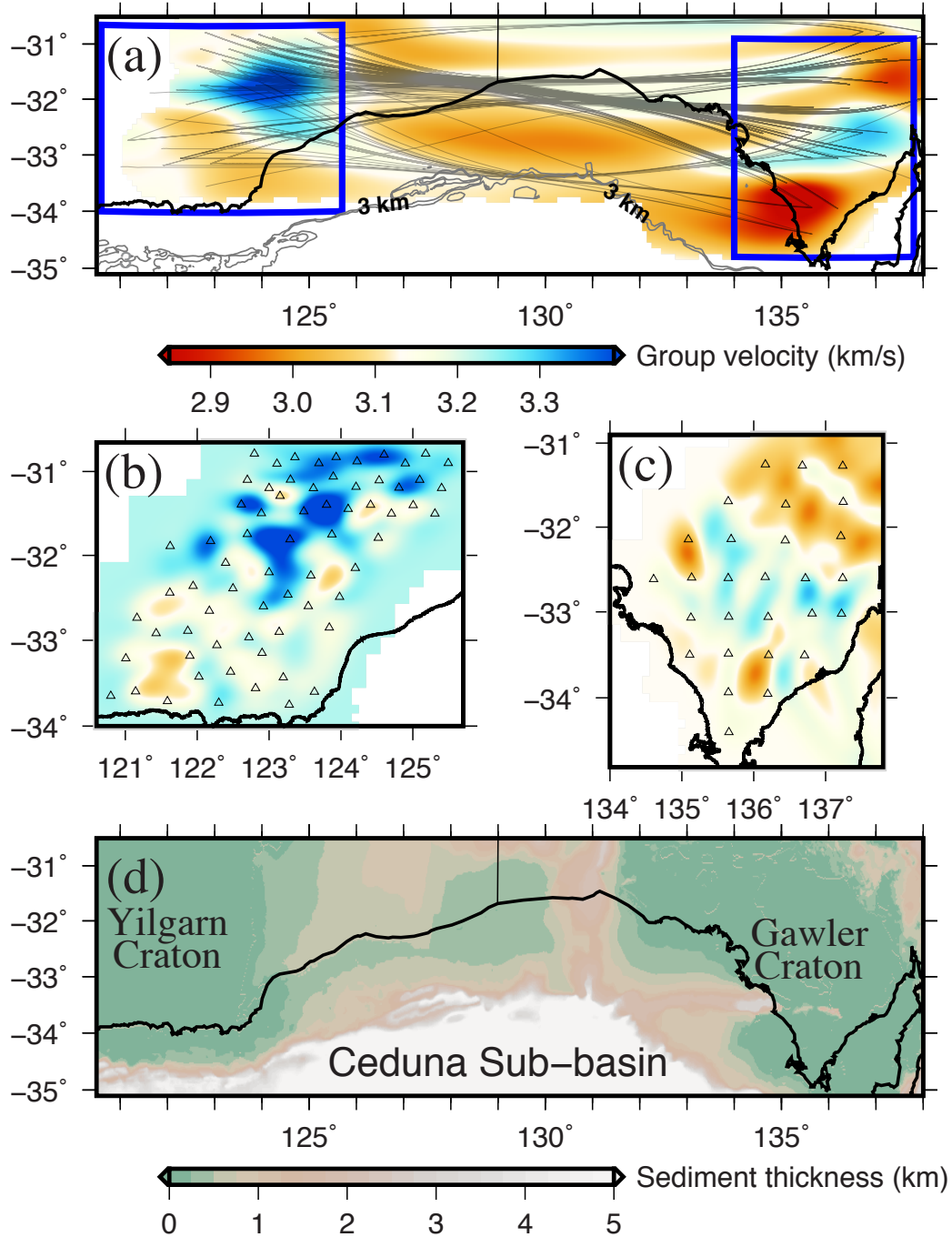


**Figure 9.** Tomographic inversion using the empirical Green's functions retrieved from  $C^1$  and  $C^2$ . (a) The group velocity tomograms at 8 sec constructed by inverting the group delays measured from the EGFs retrieved using  $C^2$  between the two temporary arrays. The locations of ALFREX and GAWLER are highlighted with the blue rectangles. The grey lines indicate the sedimentary thickness contours. The velocities beneath (b) ALFREX and (c) GAWLER inverted using  $C^1$  from the respective arrays. The station locations are indicated by the triangles. (d) The sedimentary thickness distribution near the southern Australian margins obtained from OZ Seebase model (<http://www.frogtech.com.au/ozseebase/>), providing constraints to shallow crustal structures.



271 compared to those used in the ALFREX example (see Figure 2b), clear surface wave arrivals  
 272 can be identified from the resulting  $C^2$  functions (Figure 8b). However, a direct assess-  
 273 ment of the quality of inter-array  $C^2$  is prohibited by the lack of  $C^1$  functions from the  
 274 same ray-paths. Thus, we select two permanent stations in the proximity of the respec-  
 275 tive temporary networks (Figure 8a) to compute the EGFs using  $C^1$  (Figure 8c). This  
 276 ensures, as best as possible, a similar spatial sampling to the inter-array area as that of  
 277  $C^2$ . Benefiting from a long-time ( $>1$  year) averaging of ambient noise, the SNR of  $C^1$   
 278 is higher than that of  $C^2$  which has been computed using a limited number of determin-  
 279 istic sources. The consistency between the two sets of EGFs is encouraging in view of  
 280 1) a similar move-out velocity of the surface waves and 2) the asymmetric waveforms with  
 281 a decreasing amplitude at far offsets.

282 The retrieved EGFs between the ALFREX and GAWLER networks provide new  
 283 seismic constraints to the subsurface structure of the inter-array area. This broad region  
 284 marks the complex tectonic setting of the southern Australia continental margin, where  
 285 the crustal domain transitions rapidly from the Archean Yilgarn craton in the west, through  
 286 the Proterozoic Albany-Fraser orogen and the Paleozoic offshore basin, to the Archean  
 287 Gawler craton in the east. Rayleigh wave travel times determined from  $C^2$  functions are  
 288 inverted with the fast-matching method on a regular grid with  $31 \times 31$  nodes. The result-  
 289 ing tomogram shows a strong lateral variation from the high group velocities beneath  
 290 ALFREX and GAWLER networks to a broad intervening low-velocity zone (Figure 9a).  
 291 The predominantly E-W orientated ray-paths lead to strong smearing, which prevents  
 292 an accurate assessment of the lateral scale of the size of the velocity structures. In con-  
 293 trast, the nominal resolution in the latitudinal direction is higher, delineating a sharp  
 294 velocity transition from the continental to offshore areas. The majority of rays propa-  
 295 gate along a high-velocity corridor along the continental margin (Figure 9a), a structure  
 296 that has been reported in an earlier continental-scale model (Saygin & Kennett, 2012).  
 297 We present independent constraints to the structures beneath the two arrays by invert-  
 298 ing the  $C^1$  from the respective network (i.e., intra-array EGFs). The ALFREX result  
 299 shows a high-velocity zone extending from the center towards the NE (Figure 9b). The  
 300 structure of GALWER is dominated by a core of scattered high velocities surrounded  
 301 by reduced wave speeds (Figure 9c). Similar high-velocity structures are revealed by am-  
 302 bient noise imaging using the  $C^1$  technique conducted near the Albany-Fraser orogen (Sippl  
 303 et al., 2017) and the Gawler craton (Pilia et al., 2015). The spatial distributions and rel-

304 active strength of the two high-velocity structures beneath the two arrays are highly cor-  
 305 related with those from the tomographic model inverted using the asynchronous EGFs  
 306 from  $C^2$  (Figure 9a). This broad inter-array region constitutes the offshore of the south-  
 307 ern Australian margins that has been sparsely sampled by earlier continental-scale stud-  
 308 ies (Saygin & Kennett, 2010, 2012). Several offshore basins are covered by a thick Proterozoic-  
 309 Mesozoic sedimentary sequence, varying from 2 km in the shallow marginal basin to over  
 310 15 km in the depocentre of the Ceduna Sub-basin (OZ Seebase model). The propaga-  
 311 tion of short-period (8 sec) surface waves are mainly sensitive to upper crustal hetero-  
 312 geneities. As a result, the ray-path is strongly affected by the defocusing effect of the low-  
 313 velocity structures, which generally follow the distribution of shallow (<3 km) sediment  
 314 deposits in the offshore basins (Figure 9d).

## 315 5 Discussion

### 316 5.1 Controlling factors for the quality of $C^2$

317 The two examples at different scales demonstrate that the EGFs can be robustly  
 318 retrieved from the deterministic wavefields between asynchronous stations (networks).  
 319 We discuss a few key factors that can affect the performance of  $C^2$ , including 1) the qual-  
 320 ity of  $C^1$ , 2) the azimuthal and distance distribution of the virtual sources and 3) the  
 321 relative location between a pair of asynchronous stations. Since  $C^2$  exploits the deter-  
 322 ministic surface wave energy from  $C^1$ , missing or low-quality signals in  $C^1$  inevitably lead  
 323 to poor EGF retrieval. Specifically, strong noise in  $C^1$  functions often introduces inter-  
 324 fering spurious arrivals with amplitudes comparable to that of the surface wave in  $C^2$ ,  
 325 which prevents an accurate determination of group/phase arrivals. As has been exten-  
 326 sively discussed in earlier studies (e.g., Bensen et al., 2007; Sabra et al., 2005; Stehly et  
 327 al., 2006; Yang & Ritzwoller, 2008), the quality of  $C^1$  is predominately affected by the  
 328 spatiotemporal distribution of the noise sources, and a long-term averaging of ambient  
 329 noises is often required to obtain stable  $C^1$  functions. Signal processing techniques such  
 330 as Welch’s method (Seats et al., 2012) and phase weighted stacking (Schimmel & Paulssen,  
 331 1997) can be applied to improve the convergence of  $C^1$  functions.

332 The dominating factor for obtaining high-quality EGFs using  $C^2$  is the spatial dis-  
 333 tribution of virtual sources. Unlike  $C^1$  that utilizes ambient noise without well-constrained  
 334 source locations,  $C^2$  functions are essentially constructed from a set of controlled (vir-

335 tual) sources that are collocated with the permanent stations (Figure 2). Thus, a biased  
 336 azimuthal distribution of the virtual sources (see the rose diagram in Figure 1) can pre-  
 337 clude a uniform wavefield illumination at the receiver pair of interest, a prerequisite for  
 338 the constructive stacking of EGFs (Snieder et al., 2008). This criterion is relaxed by the  
 339 stationary phase approximation, stating that only seismic sources distributed near the  
 340 inter-station path dominantly contribute to the correct arrival times, hence the construc-  
 341 tive stacking of seismic phases (Snieder, 2004; Snieder et al., 2008). In our test cases, the  
 342 virtual sources that contribute the most to  $C^2$  stacking are spatially confined within a  
 343 45-deg bin centering on the line connecting two targeting receivers, whereas non-physical  
 344 precursory energies emerge when all  $C^2$  functions are stacked without carefully select-  
 345 ing the azimuthal coverage (supplementary Figure S1). An inversion scheme that directly  
 346 utilizes these biased correlation functions has been recently investigated by Fichtner et  
 347 al. (2016). Compared to the azimuth, the effect of source-station distance on the qual-  
 348 ity of individual  $C^2$  is secondary (Figure 3). However, the far-field virtual sources are  
 349 useful to ensure the constructive stacking of  $C^2$  functions, since the stationary phase ap-  
 350 proximation is more easily fulfilled by including distant virtual sources, the result of a  
 351 wider aperture at far distances. Finally, another controlling factor is the relative loca-  
 352 tion between a pair of temporary stations subject to EGFs retrieval. The  $C^2$  achieves  
 353 the best performance when the majority of virtual sources are well aligned with the tar-  
 354 geting station pair. For example, the highest quality EGFs in the AFLREX network are  
 355 characterized by the dominating NE-SW orientated ray-paths (Figure 6c), consistent with  
 356 the direction of the densely distributed virtual sources in the NE quadrant (Figure 1a).

## 357 5.2 Comparison between $C^2$ and $C^3$ methods

358 In both test cases presented above, the  $C^3$  approach based on cross-correlation of  
 359 coda waves fails to extract consistent phase arrivals between asynchronous stations (sup-  
 360plementary Figure S2). We attribute the performance difference ( $C^2$  vs.  $C^3$ ) to the un-  
 361derlying assumptions of the seismic wavefield. The proposed  $C^2$  method exploits the in-  
 362formation carried by the deterministic part of the EGF, which is different from  $C^3$  that  
 363utilizes the diffuse coda wave energy. The application of  $C^3$  typically succeeds when sta-  
 364ble  $C^1$  functions are available from a dense seismic network (e.g., Stehly et al., 2008; Fro-  
 365ment et al., 2011; Ma & Beroza, 2012; Zhang & Yang, 2013; Spica et al., 2016, 2017; Sheng  
 366et al., 2018). In such cases, the uniformity and diffusivity of the source illuminations of



367  $C^1$  can be enhanced through the presence of (near receiver) scatters (Boschi & Weem-  
 368 stra, 2015), which produce a sufficiently diffuse scattering wavefield that is critical for  
 369 the cancellation of the cross-terms in the correlation functions (Snieder et al., 2008). How-  
 370 ever, in our study, the  $C^3$  implementation is limited by the incoherent scattering energy  
 371 in the codas that potentially arises from 1) insufficient recordings from the temporary  
 372 deployments of networks, 2) a large separation distance between the virtual source and  
 373 receiver, and/or 3) time-varying and/or a biased distribution of multiple scattering sources.  
 374 Instead, the  $C^2$  approach utilizes the deterministic energy flux (i.e., surface wave) from  
 375 a distant source, approximating a plane wave that approaches the two nearby stations  
 376 at nearly the same angle (azimuth). The accuracy of the travel-time measurements from  
 377 correlations based on the plane wave assumption has been investigated in earlier stud-  
 378 ies (Tsai, 2009; Yao & Van Der Hilst, 2009; Boschi et al., 2012) and is also demonstrated  
 379 by our tomography examples (see Figures 7 and 9). We argue that the  $C^2$  method is less  
 380 affected by the high-level waveform fluctuations in  $C^1$  codas and is more resistant to net-  
 381 work irregularity, such that a few high-quality virtual sources within the stationary phase  
 382 zone are generally sufficient to provide the unbiased EGF estimates (Figure 3).

### 383 5.3 Travel-time bias in EGFs from $C^2$

384 Travel-time bias in cross-correlation function resulting from non-isotropic source  
 385 distribution has been widely reported (e.g., Weaver et al., 2009; Tsai, 2009; Yao & Van  
 386 Der Hilst, 2009; Froment et al., 2010). The effects of virtual source distribution on travel  
 387 time are further investigated in our study. The amount of travel-time bias in the  $C^2$  func-  
 388 tion is determined by the time lag ( $\delta t$ ) that leads to the maximum correlation coefficient  
 389 between the surface waves of  $C^1$  and  $C^2$  functions from the same station pair (Figure  
 390 10a) (Froment et al., 2010). To ensure a statistically robust result, we remove large out-  
 391 liers with time lags greater than one standard deviation of the measurements, which typ-  
 392 ically result from unreliable cross-correlation measurements caused by cycle skipping or  
 393 noisy  $C^1/C^2$  functions. The cleaned dataset retains 70-90% of the raw measurements,  
 394 depending on the frequency. The resulting bias is small at shorter periods, which is on  
 395 par with the sampling rate of the cross-correlation function (0.2 sec), and increases semi-  
 396 linearly to about 0.5 sec at longer periods (Figure 10b). These travel-time biases are small  
 397 compared to the total travel times (on average 45 sec) of surface wave, hence only in-  
 398 troducing a maximum measurement uncertainty of less than 2%. For most of the mea-

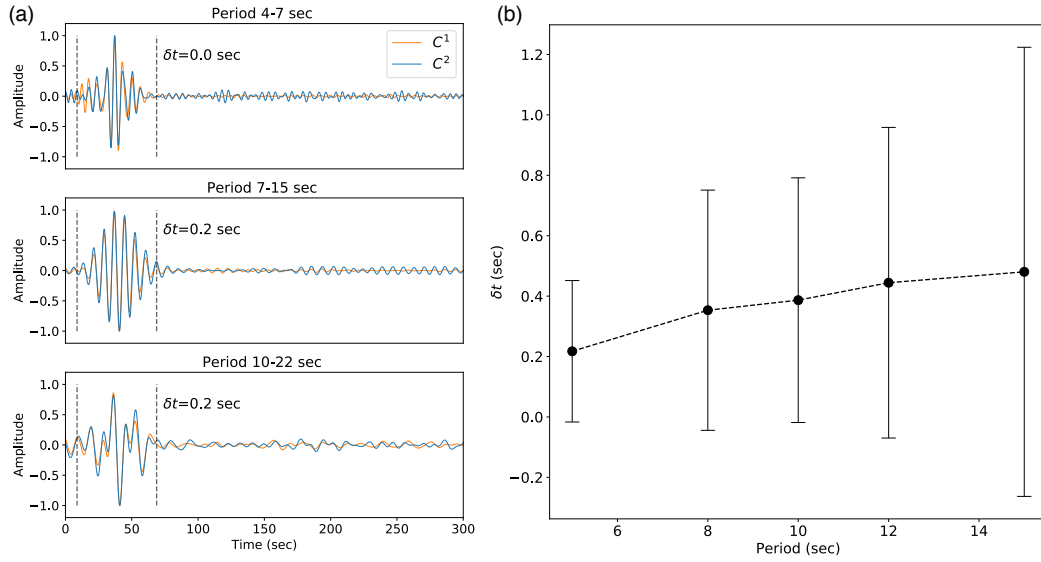


**Figure 10.** Figure 10 Measurement of the travel-time bias in  $C^2$  functions. (a) A sample measurement for station pair FA30-FB02. The EGFs obtained from  $C^1$  (orange) and  $C^2$  functions (blue) are filtered in multi-frequency bands and their relative travel-time shift ( $\delta t$ ) is labeled. The dashed lines indicate the time window of surface wave used in the analysis. (b) Travel-time bias as a function of period for all synchronous station pairs in the ALFREX network. The mean value is marked by the circle and the corresponding standard deviation is indicated by the error bar.

399 measurements, the mismatch between the  $C^1$  and  $C^2$  functions is minimal and excellent con-  
 400 sistency exists in surface waves and extends into the late codas (Figure 10a and supple-  
 401 mentary Figures S4-S11).

402 This frequency-dependent uncertainty is consistent with earlier theoretical inves-  
 403 tigations of the error in apparent travel-time in cross-correlation functions caused by far-  
 404 field anisotropic sources (Froment et al., 2010; Weaver et al., 2009). These have shown  
 405 that the predicted travel-time uncertainty decreases at shorter periods and larger inter-  
 406 station distances. In our study, we do not observe a clear dependency of travel-time bias  
 407 on distance, which may be caused by a relatively small variation in inter-station distance  
 408 ( $\sim 100$  km) compared to the length-scale of the far-field sources (in the order of thou-  
 409 sands of kilometers; Figure 1). Overall, the effect of non-isotropic wavefield intensity is  
 410 minimized by stacking the  $C^2$  functions from virtual sources that fall within the station-  
 411 ary phase zone, as validated by our tomographic examples. This non-isotropic effect can  
 412 be further reduced by the  $C^3$  method that takes advantage of the scattered wavefield (Froment  
 413 et al., 2010), which may lead to more accurate travel time estimates under an ideal net-  
 414 work configuration.

#### 415 **5.4 Relationship to source-receiver interferometry**

416 The representation of  $C^2$  is similar to source-receiver interferometry (Curtis & Hal-  
 417 liday, 2010; Curtis et al., 2012) that has been applied to reconstructing the virtual seis-  
 418 mograms between earthquake-earthquake (Curtis et al., 2009) or earthquake-station pairs  
 419 (Curtis et al., 2012; Entwistle et al., 2015). In these implementations, the actual earth-  
 420 quake response is projected to a receiver using the  $C^1$  functions between the target re-  
 421 ceiver and the backbone stations. The  $C^2$  method differs from source-receiver interfer-  
 422 ometry by replacing the earthquake with a collocated receiver that acts as a virtual source  
 423 with respect to the surrounding permanent (backbone) stations. This equivalence also  
 424 implies a change in source characteristics (depth and focal mechanism) from a complex  
 425 source-time function of an earthquake to an impulse surface response of the EGF (Denolle  
 426 et al., 2013). An earlier study extended the applicability of source-receiver interferom-  
 427 etry to inter-receiver distances over 2000 km (Entwistle et al., 2015), similar to the length-  
 428 scale investigated in our study.

## 6 Conclusion

This study presents the development of a new higher-order cross-correlation scheme ( $C^2$ ) to extract the EGFs between seismic stations operated asynchronously through deterministic wavefields. Compared to the  $C^3$  approach, the implementation of  $C^2$  is less affected by irregular network configurations and only requires a relatively short recording period of the ambient noise wavefield, hence is ideal for bridging the spatiotemporal gaps between networks deployed at different times. The retrieved EGFs are inverted to obtain group velocities at two length scales, including a regional network with asynchronous station setup and two distant networks operating 5 years apart. The accuracy of the tomographic model derived from the  $C^2$  functions is benchmarked with the results from conventional ambient noise imaging. The larger scale implementation offers new structural constraints to the previously largely undersampled offshore area of southern Australia. We conclude that  $C^2$  is a feasible and promising method for exploiting the information of existing data and improving the resolution of seismic imaging. Our study shows that the current network topology of Australia, characterized by a set of asynchronous transportable arrays covering various parts of the continent and permanent stations mostly deployed along the coastlines, offers an ideal setting to implement the  $C^2$  method. Furthermore, this technique is easily applicable to other continents. With improved data sampling, it is possible to further refine the regional and continental scale crustal models that will ultimately lead to a better understanding of the Earth's structure.

## Acknowledgments

We thank the members of Research School of Earth Sciences of the Australian National University for collecting and making the data available. We thank David Howard of GSWA for assistance on ALFREX data. We thank Mehdi Tork Qashqai, Caroline Johnson and Andrew King for reviewing an earlier version of the manuscript. The seismic data used in computing cross-correlation functions are available from IRIS DMC (<https://ds.iris.edu/ds/nodes/dmc/>) and AusPass (<http://auspass.edu.au>). Obspy (Beyreuther et al., 2010) and the Generic Mapping Tools (Wessel & Smith, 1998) are used to produce the results.

## References

Ansaripour, M., Rezapour, M., & Saygin, E. (2019). Shear wave velocity structure of

- 460 iranian plateau: Using combination of ambient noise cross-correlations (c1) and  
 461 correlation of coda of correlations (c3). *Geophysical Journal International*.
- 462 Bakulin, A., & Calvert, R. (2006). The virtual source method: Theory and case  
 463 study. *Geophysics*, *71*(4), SI139–SI150.
- 464 Bensen, G., Ritzwoller, M., Barmin, M., Levshin, A., Lin, F., Moschetti, M., . . .  
 465 Yang, Y. (2007). Processing seismic ambient noise data to obtain reliable  
 466 broad-band surface wave dispersion measurements. *Geophysical Journal Inter-*  
 467 *national*, *169*(3), 1239–1260.
- 468 Beyreuther, M., Barsch, R., Krischer, L., Megies, T., Behr, Y., & Wassermann, J.  
 469 (2010). Obspy: A python toolbox for seismology. *Seismological Research*  
 470 *Letters*, *81*(3), 530–533.
- 471 Boschi, L., & Weemstra, C. (2015). Stationary-phase integrals in the cross correla-  
 472 tion of ambient noise. *Reviews of Geophysics*, *53*(2), 411–451.
- 473 Boschi, L., Weemstra, C., Verbeke, J., Ekström, G., Zunino, A., & Giardini, D.  
 474 (2012). On measuring surface wave phase velocity from station–station cross-  
 475 correlation of ambient signal. *Geophysical Journal International*, *192*(1),  
 476 346–358.
- 477 Campillo, M., & Paul, A. (2003). Long-range correlations in the diffuse seismic coda.  
 478 *Science*, *299*(5606), 547–549.
- 479 Campillo, M., Roux, P., Romanowicz, B., & Dziewonski, A. (2014). Seismic imag-  
 480 ing and monitoring with ambient noise correlations. *Treatise on Geophysics*, *1*,  
 481 256–271.
- 482 Curtis, A., Behr, Y., Entwistle, E., Galetti, E., Townend, J., & Bannister, S. (2012).  
 483 The benefit of hindsight in observational science: Retrospective seismological  
 484 observations. *Earth and Planetary Science Letters*, *345*, 212–220.
- 485 Curtis, A., & Halliday, D. (2010). Source-receiver wave field interferometry. *Physical*  
 486 *Review E*, *81*(4), 046601.
- 487 Curtis, A., Nicolson, H., Halliday, D., Trampert, J., & Baptie, B. (2009). Virtual  
 488 seismometers in the subsurface of the earth from seismic interferometry. *Na-*  
 489 *ture Geoscience*, *2*(10), 700.
- 490 Denolle, M., Dunham, E., Prieto, G., & Beroza, G. (2013). Ground motion predic-  
 491 tion of realistic earthquake sources using the ambient seismic field. *Journal of*  
 492 *Geophysical Research: Solid Earth*, *118*(5), 2102–2118.

- 493 Entwistle, E., Curtis, A., Galetti, E., Baptie, B., & Meles, G. (2015). Constructing  
 494 new seismograms from old earthquakes: Retrospective seismology at multiple  
 495 length scales. *Journal of Geophysical Research: Solid Earth*, *120*(4), 2466–  
 496 2490.
- 497 Fichtner, A., Stehly, L., Ermert, L., & Boehm, C. (2016). Generalised  
 498 interferometry-i. theory for inter-station correlations. *Geophysical Journal  
 499 International*, ggw420.
- 500 Froment, B., Campillo, M., & Roux, P. (2011). Reconstructing the green’s function  
 501 through iteration of correlations. *Comptes Rendus Geoscience*, *343*(8-9), 623–  
 502 632.
- 503 Froment, B., Campillo, M., Roux, P., Gouedard, P., Verdel, A., & Weaver, R. L.  
 504 (2010). Estimation of the effect of nonisotropically distributed energy on the  
 505 apparent arrival time in correlations. *Geophysics*, *75*(5), SA85–SA93.
- 506 Kao, H., Behr, Y., Currie, C. A., Hyndman, R., Townend, J., Lin, F.-C., . . . He,  
 507 J. (2013). Ambient seismic noise tomography of canada and adjacent re-  
 508 gions: Part i. crustal structures. *Journal of Geophysical Research: Solid Earth*,  
 509 *118*(11), 5865–5887.
- 510 Levshin, A., & Ritzwoller, M. (2001). Automated detection, extraction, and mea-  
 511 surement of regional surface waves. In *Monitoring the comprehensive nuclear-  
 512 test-ban treaty: Surface waves* (pp. 1531–1545). Springer.
- 513 Lin, F.-C., Moschetti, M. P., & Ritzwoller, M. H. (2008). Surface wave tomogra-  
 514 phy of the western united states from ambient seismic noise: Rayleigh and  
 515 love wave phase velocity maps. *Geophysical Journal International*, *173*(1),  
 516 281–298.
- 517 Lin, F.-C., Ritzwoller, M. H., Townend, J., Bannister, S., & Savage, M. K. (2007).  
 518 Ambient noise rayleigh wave tomography of new zealand. *Geophysical Journal  
 519 International*, *170*(2), 649–666.
- 520 Lobkis, O. I., & Weaver, R. L. (2001). On the emergence of the greens function  
 521 in the correlations of a diffuse field. *The Journal of the Acoustical Society of  
 522 America*, *110*(6), 3011–3017.
- 523 Ma, S., & Beroza, G. C. (2012). Ambient-field green’s functions from asynchronous  
 524 seismic observations. *Geophysical Research Letters*, *39*(6).
- 525 Pilia, S., Rawlinson, N., Cayley, R., Bodin, T., Musgrave, R., Reading, A., . . .

- 526 Young, M. (2015). Evidence of micro-continent entrainment during crustal  
527 accretion. *Scientific reports*, *5*, 8218.
- 528 Porritt, R. W., Miller, M. S., O’Driscoll, L. J., Harris, C. W., Roosmawati, N., & da  
529 Costa, L. T. (2016). Continent–arc collision in the banda arc imaged by ambi-  
530 ent noise tomography. *Earth and Planetary Science Letters*, *449*, 246–258.
- 531 Rawlinson, N., & Kennett, B. L. (2004). Rapid estimation of relative and absolute  
532 delay times across a network by adaptive stacking. *Geophysical Journal Inter-  
533 national*, *157*(1), 332–340.
- 534 Rawlinson, N., Salmon, M., & Kennett, B. L. (2014). Transportable seismic array  
535 tomography in southeast australia: Illuminating the transition from protero-  
536 zoic to phanerozoic lithosphere. *Lithos*, *189*, 65–76.
- 537 Sabra, K. G., Gerstoft, P., Roux, P., Kuperman, W., & Fehler, M. C. (2005). Ex-  
538 tracting time-domain green’s function estimates from ambient seismic noise.  
539 *Geophysical Research Letters*, *32*(3).
- 540 Saygin, E., & Kennett, B. (2012). Crustal structure of australia from ambient  
541 seismic noise tomography. *Journal of Geophysical Research: Solid Earth*,  
542 *117*(B1).
- 543 Saygin, E., & Kennett, B. L. (2010). Ambient seismic noise tomography of aus-  
544 tralian continent. *Tectonophysics*, *481*(1-4), 116–125.
- 545 Schimmel, M., & Paulssen, H. (1997). Noise reduction and detection of weak, coher-  
546 ent signals through phase-weighted stacks. *Geophysical Journal International*,  
547 *130*(2), 497–505.
- 548 Schuster, G. (2009). *Seismic interferometry* (Vol. 1). Cambridge University Press  
549 Cambridge.
- 550 Schuster, G., Yu, J., Sheng, J., & Rickett, J. (2004). Interferometric/daylight seismic  
551 imaging. *Geophysical Journal International*, *157*(2), 838–852.
- 552 Seats, K. J., Lawrence, J. F., & Prieto, G. A. (2012). Improved ambient noise cor-  
553 relation functions using welch s method. *Geophysical Journal International*,  
554 *188*(2), 513–523.
- 555 Shapiro, N. M., & Campillo, M. (2004). Emergence of broadband rayleigh waves  
556 from correlations of the ambient seismic noise. *Geophysical Research Letters*,  
557 *31*(7).
- 558 Sheng, Y., Nakata, N., & Beroza, G. C. (2018). On the nature of higher-order am-

- 559           bient seismic field correlations. *Journal of Geophysical Research: Solid Earth*,  
560           123(9), 7969–7982.
- 561   Sippl, C., Kennett, B., Tkalčić, H., Gessner, K., & Spaggiari, C. (2017). Crustal sur-  
562           face wave velocity structure of the east albany-fraser orogen, western australia,  
563           from ambient noise recordings. *Geophysical Journal International*, 210(3),  
564           1641–1651.
- 565   Snieder, R. (2004). Extracting the greens function from the correlation of coda  
566           waves: A derivation based on stationary phase. *Physical Review E*, 69(4),  
567           046610.
- 568   Snieder, R., & Larose, E. (2013). Extracting earth’s elastic wave response from noise  
569           measurements. *Annual Review of Earth and Planetary Sciences*, 41, 183–206.
- 570   Snieder, R., Van Wijk, K., Haney, M., & Calvert, R. (2008). Cancellation of spuri-  
571           ous arrivals in greens function extraction and the generalized optical theorem.  
572           *Physical Review E*, 78(3), 036606.
- 573   Spica, Z., Perton, M., & Beroza, G. C. (2017). Lateral heterogeneity imaged by  
574           small-aperture scs retrieval from the ambient seismic field. *Geophysical Re-*  
575           *search Letters*, 44(16), 8276–8284.
- 576   Spica, Z., Perton, M., Calò, M., Legrand, D., Córdoba-Montiel, F., & Iglesias, A.  
577           (2016). 3-d shear wave velocity model of mexico and south us: bridging seismic  
578           networks with ambient noise cross-correlations (c1) and correlation of coda of  
579           correlations (c3). *Geophysical Journal International*, 206(3), 1795–1813.
- 580   Stehly, L., Campillo, M., Froment, B., & Weaver, R. L. (2008). Reconstructing  
581           green’s function by correlation of the coda of the correlation (c3) of ambient  
582           seismic noise. *Journal of Geophysical Research: Solid Earth*, 113(B11).
- 583   Stehly, L., Campillo, M., & Shapiro, N. (2006). A study of the seismic noise from  
584           its long-range correlation properties. *Journal of Geophysical Research: Solid*  
585           *Earth*, 111(B10).
- 586   Stehly, L., Fry, B., Campillo, M., Shapiro, N., Guilbert, J., Boschi, L., & Giardini,  
587           D. (2009). Tomography of the alpine region from observations of seismic  
588           ambient noise. *Geophysical Journal International*, 178(1), 338–350.
- 589   Tsai, V. C. (2009). On establishing the accuracy of noise tomography travel-time  
590           measurements in a realistic medium. *Geophysical Journal International*,  
591           178(3), 1555–1564.



- 592 Wapenaar, K., Draganov, D., Snieder, R., Campman, X., & Verdel, A. (2010). Tu-  
 593 torial on seismic interferometry: Part 1 basic principles and applications. *Geo-*  
 594 *physics*, *75*(5), 75A195–75A209.
- 595 Ward, K. M., Porter, R. C., Zandt, G., Beck, S. L., Wagner, L. S., Minaya, E., &  
 596 Tavera, H. (2013). Ambient noise tomography across the central andes. *Geo-*  
 597 *physical Journal International*, *194*(3), 1559–1573.
- 598 Weaver, R., Froment, B., & Campillo, M. (2009). On the correlation of non-  
 599 isotropically distributed ballistic scalar diffuse waves. *The Journal of the*  
 600 *Acoustical Society of America*, *126*(4), 1817–1826.
- 601 Weaver, R., & Lobkis, O. (2001). Ultrasonics without a source: Thermal fluctuation  
 602 correlations at mhz frequencies. *Physical Review Letters*, *87*(13), 134301.
- 603 Wessel, P., & Smith, W. H. (1998). New, improved version of generic mapping tools  
 604 released. *Eos, Transactions American Geophysical Union*, *79*(47), 579–579.
- 605 Yang, Y., & Ritzwoller, M. H. (2008). Characteristics of ambient seismic noise as  
 606 a source for surface wave tomography. *Geochemistry, Geophysics, Geosystems*,  
 607 *9*(2).
- 608 Yang, Y., Ritzwoller, M. H., Levshin, A. L., & Shapiro, N. M. (2007). Ambient noise  
 609 rayleigh wave tomography across europe. *Geophysical Journal International*,  
 610 *168*(1), 259–274.
- 611 Yao, H., & Van Der Hilst, R. D. (2009). Analysis of ambient noise energy distribu-  
 612 tion and phase velocity bias in ambient noise tomography, with application to  
 613 se tibet. *Geophysical Journal International*, *179*(2), 1113–1132.
- 614 Yao, H., van Der Hilst, R. D., & De Hoop, M. V. (2006). Surface-wave array tomog-  
 615 raphy in se tibet from ambient seismic noise and two-station analysisi. phase  
 616 velocity maps. *Geophysical Journal International*, *166*(2), 732–744.
- 617 Zhang, J., & Yang, X. (2013). Extracting surface wave attenuation from seismic  
 618 noise using correlation of the coda of correlation. *Journal of Geophysical Re-*  
 619 *search: Solid Earth*, *118*(5), 2191–2205.